

# One minute parity lifetime of a NbTiN Cooper-pair transistor

David J. van Woerkom<sup>†</sup>, Attila Geresdi<sup>\*†</sup> and Leo P. Kouwenhoven

The parity modulation of the ground state of a superconducting island is a direct consequence of the presence of the Cooper-pair condensate preferring an even number of charge carriers<sup>1,2</sup>. The addition energy of an odd, unpaired quasiparticle equals the superconducting gap,  $\Delta$ , suppressing single-electron hopping in the low-temperature limit,  $k_B T \ll \Delta$ . Controlling the quasiparticle occupation is of fundamental importance for superconducting qubits as single-electron tunnelling results in decoherence<sup>3,4</sup>. In particular, topological quantum computation relies on the parity control and readout of Majorana bound states<sup>5,6</sup>. Here we present the first parity modulation of a niobium titanite nitride (NbTiN) Cooper-pair transistor coupled to aluminium (Al) leads. We show that this circuit is compatible with the magnetic field requirement  $B \sim 100$  mT of inducing topological superconductivity in spin-orbit-coupled nanowires<sup>7-9</sup>. Our observed parity lifetime exceeding 1 min is several orders of magnitude higher than the required gate time for flux-controlled braiding of Majorana states<sup>10</sup>.

Experimentally, the parity modulation of a superconducting island can be observed via the ground state charge<sup>2</sup>, the even-odd modulation of the charge stability diagram<sup>11,12</sup>, or the parity dependence of the switching current,  $I_{sw}$  (refs 13,14). The interplay of the charging energy  $E_c = e^2/2C$  and the Josephson coupling energy  $E_J = I_c \hbar/2e$  where  $I_c$  is the critical current makes the Cooper-pair transistor (CPT) a single, gate-modulated Josephson junction<sup>13,15</sup> with a  $2e$  charge periodicity in the absence of parity switches—meaning, infinitely long parity lifetime,  $\tau_p$ .

Recent, direct measurements of  $\tau_p$  (refs 4,16) yielded values up to the millisecond regime for aluminium devices. Despite considerable efforts, however, no  $2e$  periodicity has been reported for non-aluminium superconductors<sup>17,18</sup>, such as niobium or vanadium. Comparative studies of aluminium and niobium CPTs suggested that the elusiveness of parity effects is related to the material properties<sup>18</sup>, in particular the formation of a surface oxide layer under ambient conditions. Whereas aluminium tends to form a few-nanometre-thick insulating oxide layer<sup>19</sup>, niobium is prone to oxidize through the bulk material<sup>20</sup>, mostly forming metallic  $\text{NbO}_x$  compounds. This process then leads to localized metallic states in the island, which prevents parity control.

In contrast, nitridized niobium compounds, such as niobium titanite nitride (NbTiN), have been shown to be less prone to form oxides<sup>20</sup> and hence are good candidates for parity-conserving superconducting circuits. Furthermore, NbTiN forms transparent contacts with spin-orbit coupled semiconductor nanowires<sup>9</sup>, and has become a preferred superconductor to investigate Majorana bound states.

Our device features a NbTiN island sputtered onto Al leads (Fig. 1a). The tunnel barriers between the island and the leads

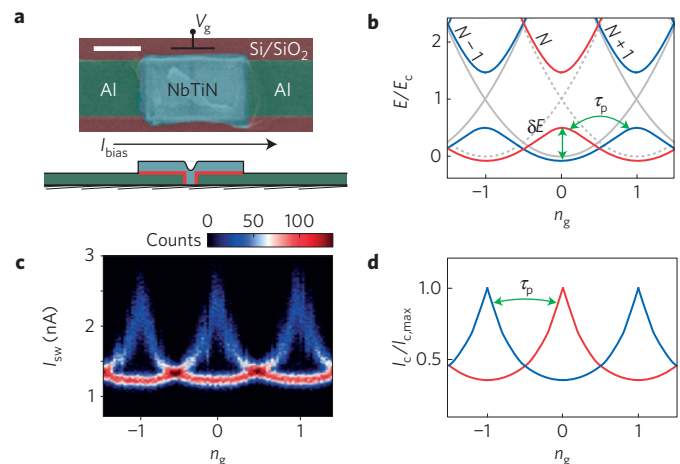


**Figure 1 | Device layout and parity-dependent switching current.**

**a**, Scanning electron microscope image and schematic cross-section of a typical Al/NbTiN/Al hybrid Cooper-pair transistor (CPT). The NbTiN island dimensions are  $250 \text{ nm} \times 450 \text{ nm}$ . Scale bar denotes  $200 \text{ nm}$ . The  $\text{AlO}_x$  oxide barriers are indicated by thick red lines. **b**, Energy level diagram as a function of the gate charge,  $n_g$ , in the presence of low-energy subgap states restoring  $1e$  periodicity. The maximum even-odd energy difference is denoted by  $\delta E$ . Grey lines represent energy levels in the absence of Josephson coupling,  $E_J = 0$ . Red and blue lines show energy levels for even and odd charge parity, respectively, both for  $E_J = E_c$ . Parity switches occur on a timescale of  $\tau_p$  owing to quasiparticle tunnelling. **c,d**, Measured switching current histogram (**c**) and calculated  $I_c(n_g)$  (**d**) in the low-temperature limit. Note that in **d** the two possible  $I_c(n_g)$  values corresponding to the even and odd charge states are denoted by blue and red lines, respectively. In the measured data (**c**) the two branches are superimposed, see text.

are created by means of controlled *in situ* surface oxidation of Al, resulting in amorphous  $\text{AlO}_x$  barriers<sup>19</sup>.

We extract a charging energy  $E_c \approx 50 \mu\text{eV}$  and  $E_J \approx 30\text{--}50 \mu\text{eV}$  for different devices. A detailed list of parameters and characterization methods are presented in the Supplementary Methods. Our devices are in the intermediate coupling regime with  $E_J \sim E_c$ , where the energy diagram (Fig. 1b) and the critical current (Fig. 1d) are sensitive to the charge parity. It is important to note that our CPTs are in the optimal regime to establish flux-controlled braiding of Majorana bound states with  $E_J \sim E_c \gg k_B T$  (ref. 10), and hence a useful platform to establish the parity lifetime for Majorana circuits<sup>21</sup>.

We model the CPT as a two-level system which can exist in either parity state (red and blue bands in Fig. 1, respectively), and

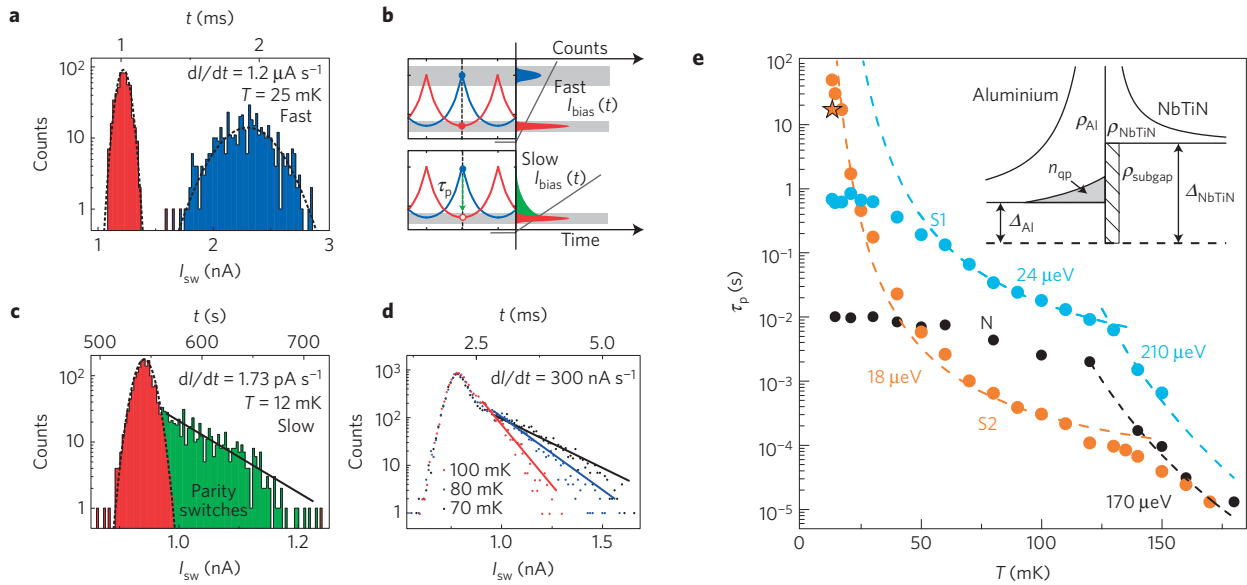


**Figure 2 | Characterization and temperature dependence of the parity lifetime.** **a**, Linecut histogram at integer  $n_g$  of Fig. 1c showing a bimodal distribution. We attribute the two peaks to the two parity states of the CPT (coloured red and blue, respectively). **b**, Schematic representation of our model. For a fast current ramp (upper panel), the histograms of the two parity states are independently probed, showing the characteristics of data in **a**. In the slow limit (lower panel), parity switches occur during the current ramp, leading to an exponential tail of the distribution (shown in green), quantifying  $\tau_p$ . The  $I_{\text{bias}}(t)$  current ramp is represented by a dark grey line. **c**, Experimental data set in the slow limit. Note the change in the current- and timescale compared with **a**. We show the exponential cutoff in green, and extract  $\tau_p = 49$  s (solid black line). The dashed black lines are guide to the eye envelopes for the peaks in **a** and **c**. **d**, Experimental data at different temperatures show the temperature dependence of  $\tau_p$ . **e**,  $\tau_p$  as a function of temperature for non-shielded device N, and shielded devices S1, S2. For detailed comparison, see the main text and the Supplementary Methods. All CPTs exhibit an activated behaviour with  $\Delta \approx 170\text{--}210$   $\mu\text{V}$  in the high-temperature limit, corresponding to the gap of the aluminium leads. Saturation of device N without shielding and no quasiparticle traps is observed below  $T \approx 100$  mK. Shielded devices S1 and S2 exhibit a minigap-activated behaviour  $\Delta^* \approx 20$   $\mu\text{V}$  in the low-temperature limit. The fitted  $\tau_p(T)$  function is defined in the main text. Star symbol shows  $\tau_p = 15$  s at  $T = 12$  mK extracted from parity-distilled data for device S2 (see Fig. 3d).

switches state on the timescale of  $\tau_p$  (ref. 22) owing to quasiparticle tunnelling. We collect the switching current histograms by repetitively sweeping the bias current from zero (non-dissipative state) to beyond the switching current. Here, in the resistive state, quasiparticle tunnelling causes a random reinitialization of the parity state of the CPT for the next measurement. This results in the apparent  $1e$  periodicity in Fig. 1c. Nevertheless, as long as the parity remains constant during each sweep, we expect to find the two branches as a bimodal histogram, as we indeed observe in Fig. 2a. In these measurements, the current ramp time is much shorter than the parity lifetime,  $\tau_p$  (fast measurement limit).

We quantify  $\tau_p$  in the slow measurement limit. In this regime parity switches occur during the current ramp (Fig. 2b lower panels) such that reaching the upper branch (depicted as blue in Fig. 2a,b) becomes exponentially suppressed (Fig. 2c). The exponential tail represents parity switches during the current bias ramp, resulting in an observable decay of the upper branch (depicted as green in Fig. 2b,c),  $p_u(t) = p_u(0) \exp(-t/\tau_p)$ . Thus, from the decay of the histogram (black solid line in Fig. 2c), we can directly obtain  $\tau_p$ .

The observed  $\tau_p$  is a result of single-electron tunnelling events through the junctions of the CPT. In the zero-voltage state, we can link  $\tau_p$  to  $\rho_{\text{subgap}}$ , the subgap density of states on the island, and  $n_{\text{qp}}$ , the quasiparticle density in the leads (for details see the Supplementary Methods):

$$\tau_p^{-1} = \frac{2n_{\text{qp}}}{e^2 R_N \rho_{\text{Al}}} \frac{\rho_{\text{subgap}}}{\rho_{\text{NbTiN}}} \quad (1)$$

where  $R_N$  is the normal state resistance of the CPT. It is instructive to note that equation (1) is similar to the tunnelling rate derived in ref. 23 for a device with a normal metallic island, which stems from our assumption of a finite subgap density of states

in the island. In our case, the parity lifetime is determined by the quasiparticle density in the leads<sup>21</sup> and the phenomenological Dynes parameter<sup>24</sup>,  $\rho_{\text{subgap}}/\rho_{\text{NbTiN}}$ , of the island material. Assuming a thermal quasiparticle density

$$n_{\text{qp}}(T) = \rho_{\text{Al}} \sqrt{2\pi k_B T \Delta_{\text{Al}}} e^{-\frac{\Delta_{\text{Al}}}{k_B T}} \quad (2)$$

in the leads, we find  $\Delta_{\text{Al}} \approx 170\text{--}210$   $\mu\text{V}$  (Fig. 2e) for temperatures exceeding 120 mK, in good agreement with the superconducting gap of the aluminium leads extracted from the charge stability diagram. Furthermore, by inserting equation (2) into equation (1), we get an estimate of the Dynes parameter to be  $\sim 10^{-2}$ . This is in good agreement with the value of  $\sim 10^{-3}$  that we get based on our measurements of a single NbTiN/AlO<sub>x</sub>/Al junction shown in the Supplementary Methods. We can therefore attribute the observed parity lifetime for  $T > 120$  mK to the thermal quasiparticle population in the leads.

For device N, however, we find a saturated  $\tau_p = 9.5$  ms in the low-temperature limit, a common observation in superconducting qubits<sup>4</sup> and hybrid single-electron transistors<sup>23</sup> signifying the presence of non-thermal quasiparticle excitations.

A common strategy to drain non-thermal quasiparticles is to introduce traps—normal metal junctions attached to the leads. We note that the trapping efficiency of a quasiparticle trap is influenced by its distance from the CPT with respect to the quasiparticle diffusion length on the timescale of the recombination time<sup>25</sup>. Our choice of a nominal 5  $\mu\text{m}$  separation is much shorter than the typical diffusion length of  $\gtrsim 100$   $\mu\text{m}$ , even at the highest temperature of  $T = 150$  mK. However, as this distance is much longer than the estimated coherence length of  $\xi_{\text{Al}} \approx 100$  nm, the inverse proximity effect does not influence the transport at the junction of the CPT (ref. 26).

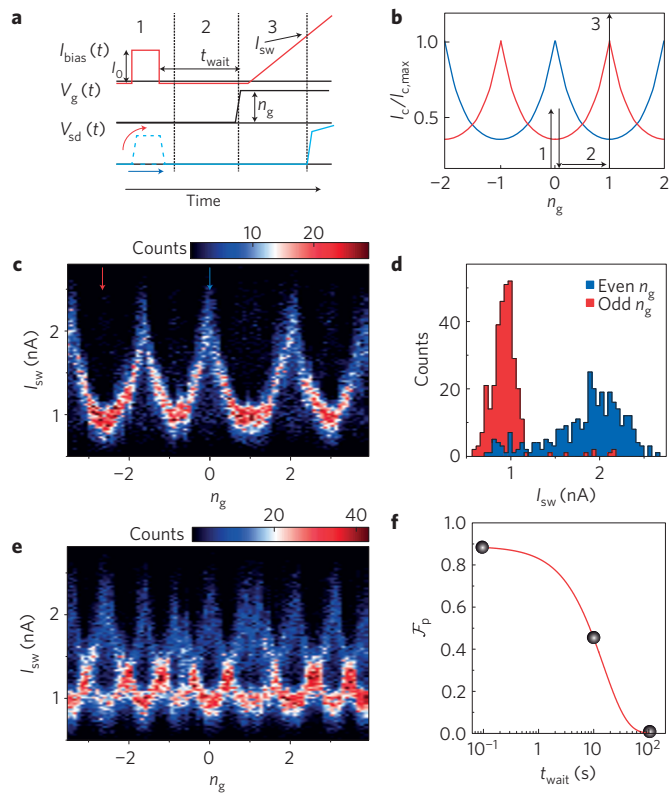


**Figure 3 | Parity-state distillation.** **a**, Schematic current bias and gate voltage waveforms applied to the device. First, a current bias pulse with an amplitude between the two branches is applied (1). At the same time the measured voltage  $V_{sd}(t)$  is recorded to initialize the parity state. Then the gate voltage is ramped (2) and, finally, the switching current is recorded (3). **b**, Schematic representation of the applied waveforms overlaid on the parity-dependent critical current. **c**, Parity-distilled switching current histogram exhibiting  $2e$  periodicity with the wait time  $t_{wait} = 100$  ms. **d**, Linecut histograms for an even (blue) and odd (red)  $n_g$  at the positions denoted by arrows in **c**. **e**, Raw histogram without parity distillation exhibiting  $1e$  periodicity. Slight shifts in **c** and **e** are caused by gate charge switches that occur on a timescale of several 10 min. **f**, Parity-distillation fidelity as a function of  $t_{wait}$ , see main text. Solid red line denotes the fit  $\sim \exp(-t_{wait}/\tau_p)$  with  $\tau_p = 15$  s. All data was recorded on device S2.

By introducing quasiparticle traps and microwave-tight shielding coated with infrared absorber painting for devices S1 and S2, we find a non-saturated behaviour of  $\tau_p$  (Fig. 2e). We observe a minigap-activated temperature dependence with  $\Delta^* \approx 20 \mu\text{eV}$  for both devices, which we attribute to a minimum excitation energy on the island. This activation energy is consistent with the maximum even-odd energy difference of  $\delta E \approx 20\text{--}30 \mu\text{eV}$  (Fig. 1b), which promotes  $\tau_p \sim \exp(\delta E/k_B T)$  (ref. 27).

It is to be stressed that the lack of saturation signals that the effective quasiparticle temperature of the CPT follows the bath temperature down to the 10 mK regime, which is in clear contrast to the saturated behaviour of device N. We find  $\tau_p = 49$  s at  $T = 12$  mK for device S2. To put this number into context, we note that the Josephson frequency  $f_J = E_J/h \approx 10$  GHz and thus a single-quasiparticle event occurs only once for every  $\tau_p f_J \sim 10^{11}$  Cooper pairs tunnelling through the junctions. This signifies the low probability of parity switches for an open device with  $E_J \approx E_c$  required for flux-tunable Majorana braiding schemes.

Thus far, we started each switching current measurement from an unknown parity state because of the random reinitialization in the dissipative state of the CPT for  $I_{bias} > I_{sw}$ . To reproducibly select the

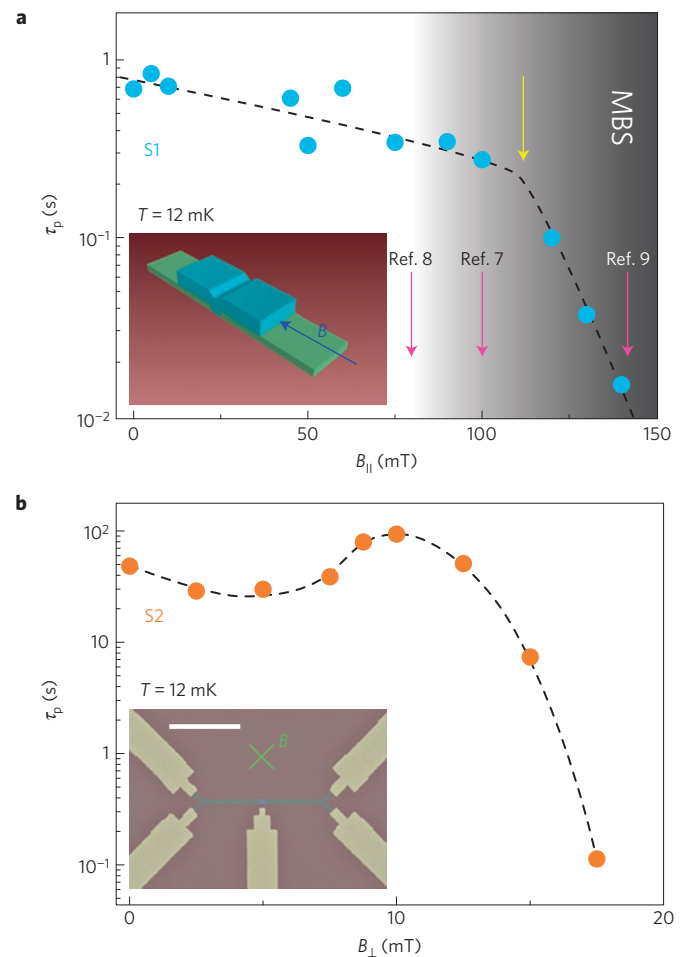


**Figure 4 | Influence of the magnetic field on the CPT.** **a, b**, The parity lifetime as a function of in-plane field,  $B_{\parallel}$  (**a**) and perpendicular field,  $B_{\perp}$  (**b**), respectively. In **a**, the shaded region and the purple arrows depict the condition for inducing Majorana bound states (MBS) in spin-orbit-coupled semiconductor wires<sup>7–9</sup> and the yellow arrow shows the onset of the steeper decay at  $B_{\parallel} \approx 110$  mT. The inset depicts the relative orientation of the CPT with respect to the magnetic field. In **b**, the inset shows the false-colour electron microscope image of the device, with the white scale bar denoting  $5 \mu\text{m}$ . In both panels, the dashed lines serve as a guide to the eye.

same parity state, we employ a parity-distillation protocol (Fig. 3) where, by selecting a single parity state without switching to the resistive state, we ensure that the parity remains well defined for the subsequent measurement. This protocol indeed results in a  $2e$  periodic switching current pattern (Fig. 3c), which is observed for the first time for a non-aluminium CPT.

We quantify the effectiveness of the parity distillation by defining the fidelity as:

$$\mathcal{F}_p = \frac{p_{uf} - p_{ui}}{1 - p_{ui}} \quad (3)$$

where  $p_{uf}$  is the conditional probability of the upper branch in the final step (3), and  $p_{ui}$  is the initial probability. We note that the above expression is valid for an arbitrary  $0 < p_{ui} < 1$  value set by the average quasiparticle occupation of the CPT. For device S2 we find  $\mathcal{F}_p = 0.88 \pm 0.05$  for  $t_{wait} = 100$  ms, demonstrating the high degree of parity distillation (Fig. 3d). By changing  $t_{wait}$  between the parity initialization (1) and measurement (3), we acquire an independent measurement  $\tau_p = 15$  s for device S2 at  $T = 12$  mK (Fig. 3f).

Finally, we investigate the evolution of  $\tau_p(B)$  in different magnetic field directions. In parallel magnetic field, we observe a gradual decrease of  $\tau_p$ . The onset of the steep decay at  $B_{\parallel} = 110$  mT (yellow arrow in Fig. 4a) is in agreement with the condition for vortex penetration through a mesoscopic superconducting island<sup>28</sup> with  $\Phi \approx 1.1\Phi_0 \gtrsim \Phi_0$ , where  $\Phi_0 = h/2e$  is the magnetic flux quantum. We note that the measurement geometry shown in the inset of Fig. 4a may give rise to a Fraunhofer-like interference on the same magnetic field scale; however, the upper critical magnetic field of 320 mT of the Al leads did not allow the evaluation of  $\tau_p$  over a larger magnetic field range—that is, several flux quanta.

These results underline the significance of the sample geometry of the CPTs in maintaining parity control in a finite magnetic field. However, our device exhibits  $\tau_p > 10$  ms in  $B_{\parallel} > 100$  mT, required to induce Majorana bound states<sup>9</sup>.

In contrast, applying a perpendicular field first results in an increase of  $\tau_p$ , reaching a maximum value  $\tau_p = 94$  s at  $B_{\perp} \approx 10$  mT, before dropping at higher magnetic fields (Fig. 4b). Notably, the typical switching current values, shown in the Supplementary Methods, do not follow the same trend. Making use of the relation between the lower critical field and the stripe width,  $B_{c1,\perp}(w) \sim \Phi_0/w^2$  (ref. 29), we attribute the initial increase to vortex formation and hence more effective quasiparticle trapping in the wide lead sections ( $w \approx 2 \mu\text{m}$ ) of the device (see the yellow sections in the inset of Fig. 4b). On reaching  $B_{\perp} \approx 10$  mT, the vortex phase becomes stable in the close vicinity of the CPT ( $w \approx 250$  nm), causing a gradual decrease of  $\tau_p$ . We note that owing to  $\xi_{\text{Al}} \approx 100$  nm  $\sim w$  for our devices, we cannot make a quantitative comparison between our measurement data and theoretical expressions for the critical magnetic field of thin stripes. However, we conclude that vortices induced by a perpendicular magnetic field can increase the efficiency of quasiparticle traps, but the formation of a vortex phase in the near vicinity of the CPT enhances quasiparticle transport in agreement with earlier observations<sup>29,30</sup>.

## Methods

Methods and any associated references are available in the [online version of the paper](#).

Received 15 January 2015; accepted 22 April 2015;  
published online 25 May 2015

## References

1. Averin, D. & Nazarov, Yu. Single-electron charging of a superconducting island. *Phys. Rev. Lett.* **69**, 1993–1996 (1992).
2. Lafarge, P., Joyez, P., Esteve, D., Urbina, C. & Devoret, M. H. Two-electron quantization of the charge on a superconductor. *Nature* **365**, 422–424 (1993).
3. Clarke, J. & Wilhelm, F. K. Superconducting quantum bits. *Nature* **453**, 1031–1042 (2008).
4. Riste, D. *et al.* Millisecond charge-parity fluctuations and induced decoherence in a superconducting transmon qubit. *Nature Commun.* **4**, 1913 (2013).
5. Alicea, J. New directions in the pursuit of Majorana fermions in solid state systems. *Rep. Prog. Phys.* **75**, 076501 (2012).
6. Read, N. Topological phases and quasiparticle braiding. *Phys. Today* **65**, 38–43 (July, 2012).
7. Lutchyn, R. M., Sau, J. D. & Das Sarma, S. Majorana fermions and a topological phase transition in semiconductor–superconductor heterostructures. *Phys. Rev. Lett.* **105**, 077001 (2010).
8. Oreg, Y., Refael, G. & von Oppen, F. Helical liquids and Majorana bound states in quantum wires. *Phys. Rev. Lett.* **105**, 177002 (2010).
9. Mourik, V. *et al.* Signatures of Majorana fermions in hybrid superconductor–semiconductor nanowire devices. *Science* **336**, 1003–1007 (2012).
10. Hyart, T. *et al.* Flux-controlled quantum computation with Majorana fermions. *Phys. Rev. B* **88**, 035121 (2013).

11. Tuominen, M. T., Hergenrother, J. M., Tighe, T. S. & Tinkham, M. Experimental evidence for parity-based  $2e$  periodicity in a superconducting single-electron tunneling transistor. *Phys. Rev. Lett.* **69**, 1997–2000 (1992).
12. Eiles, T., Martinis, J. & Devoret, M. Even–odd asymmetry of a superconductor revealed by the Coulomb blockade of Andreev reflection. *Phys. Rev. Lett.* **70**, 1862–1865 (1993).
13. Joyez, P., Lafarge, P., Filipe, A., Esteve, D. & Devoret, M. H. Observation of parity-induced suppression of Josephson tunneling in the superconducting single electron transistor. *Phys. Rev. Lett.* **72**, 2458–2461 (1994).
14. Aumentado, J., Keller, M. W., Martinis, J. M. & Devoret, M. H. Nonequilibrium quasiparticles and  $2e$  periodicity in single-Cooper-pair transistors. *Phys. Rev. Lett.* **92**, 066802 (2004).
15. Geerligs, L. J., Anderegg, V. F., Romijn, J. & Mooij, J. E. Single Cooper-pair tunneling in small-capacitance junctions. *Phys. Rev. Lett.* **65**, 377–380 (1990).
16. Shaw, M. D., Lutchyn, R. M., Delsing, P. & Echternach, P. M. Kinetics of nonequilibrium quasiparticle tunneling in superconducting charge qubits. *Phys. Rev. B* **78**, 024503 (2008).
17. Dolata, R., Scherer, H., Zorin, A. B. & Niemeyer, J. Single-charge devices with ultrasmall Nb/AIO<sub>x</sub>/Nb trilayer Josephson junctions. *J. Appl. Phys.* **97**, 054501 (2005).
18. Savin, A. M. *et al.* Parity effect in Al and Nb single electron transistors in a tunable environment. *Appl. Phys. Lett.* **91**, 063512 (2007).
19. Oliver, W. D. & Welander, P. B. Materials in superconducting quantum bits. *Mater. Res. Soc. Bull.* **38**, 816–825 (2013).
20. Darlinski, A. & Halbritter, J. Angle-resolved XPS studies of oxides at NbN, NbC, and Nb surfaces. *Surf. Interface Anal.* **10**, 223–237 (1987).
21. Rainis, D. & Loss, D. Majorana qubit decoherence by quasiparticle poisoning. *Phys. Rev. B* **85**, 174533 (2012).
22. Lutchyn, R. M., Glazman, L. I. & Larkin, A. I. Kinetics of the superconducting charge qubit in the presence of a quasiparticle. *Phys. Rev. B* **74**, 064515 (2006).
23. Saira, O.-P., Kemppinen, A., Maisi, V. F. & Pekola, J. P. Vanishing quasiparticle density in a hybrid Al/Cu/Al single-electron transistor. *Phys. Rev. B* **85**, 012504 (2012).
24. Dynes, R., Narayanamurti, V. & Garno, J. Direct measurement of quasiparticle-lifetime broadening in a strong-coupled superconductor. *Phys. Rev. Lett.* **41**, 1509–1512 (1978).
25. Rajauria, S. *et al.* Efficiency of quasiparticle evacuation in superconducting devices. *Phys. Rev. B* **85**, 020505 (2012).
26. Kaupilla, V. J., Nguyen, H. Q. & Heikkilä, T. T. Nonequilibrium and proximity effects in superconductor–normal metal junctions. *Phys. Rev. B* **88**, 075428 (2013).
27. Court, N. A., Ferguson, A. J., Lutchyn, R. & Clark, R. G. Quantitative study of quasiparticle traps using the single-Cooper-pair transistor. *Phys. Rev. B* **77**, 100501 (2008).
28. Moshchalkov, V. V. *et al.* Effect of sample topology on the critical fields of mesoscopic superconductors. *Nature* **373**, 319–322 (1995).
29. Peltonen, J. T., Muhonen, J. T., Meschke, M., Kopnin, N. B. & Pekola, J. P. Magnetic-field-induced stabilization of nonequilibrium superconductivity in a normal-metal/insulator/superconductor junction. *Phys. Rev. B* **84**, 220502 (2011).
30. Wang, C. *et al.* Measurement and control of quasiparticle dynamics in a superconducting qubit. *Nature Commun.* **5**, 5836 (2014).

## Acknowledgements

The authors thank A. R. Akhmerov, S. Rubbert, Y. Nazarov, R. Lutchyn and J. Pekola for fruitful discussions and R. N. Schouten for technical assistance. This work has been supported by the Netherlands Foundation for Fundamental Research on Matter (FOM) and Microsoft Corporation Station Q. A. G. acknowledges funding from the Netherlands Organisation for Scientific Research (NWO) through a VENI grant.

## Author contributions

D.J.v.W. fabricated the devices. D.J.v.W. and A.G. performed the measurements. D.J.v.W., A.G. and L.P.K. discussed the data, contributed to the analysis and wrote the manuscript.

## Additional information

Supplementary information is available in the [online version of the paper](#). Reprints and permissions information is available online at [www.nature.com/reprints](http://www.nature.com/reprints). Correspondence and requests for materials should be addressed to A.G.

## Competing financial interests

The authors declare no competing financial interests.

## Methods

**Device fabrication.** The Cooper-pair transistors (CPTs) were fabricated using electron beam lithography and thin film deposition, starting with a  $p^{++}$  doped silicon wafer with a 285-nm-thick thermally grown  $\text{SiO}_2$  surface layer. First, aluminium leads were defined and evaporated in a high-vacuum chamber ( $p_{\text{base}} \sim 10^{-7}$  torr) at a rate of  $0.2 \text{ nm s}^{-1}$  with a thickness of 30–35 nm. Subsequently, the mask for the NbTiN island was defined in a second lithography step. The sample was loaded into an ultrahigh vacuum AJA International ATC 1800 sputtering system ( $p_{\text{base}} \sim 10^{-9}$  torr), where first a  $\sim 5$  nm Al layer was removed by means of argon plasma etching at  $p = 3$  mtorr. This step was followed by *in situ* oxidation to create  $\text{AlO}_x$  tunnel barriers. Without breaking vacuum, the NbTiN island was then sputtered with a layer thickness of 70–100 nm.

We used a  $\text{Nb}_{0.7}\text{Ti}_{0.3}$  target with a diameter of 3 inches. Reactive sputtering resulting in nitrized NbTiN films was performed in an Ar/N process gas with a typical 10 at% nitrogen content at a pressure of 3 mtorr using a d.c. magnetron source. During deposition, a  $-45$  V bias was applied to the sample with respect to the target. The critical temperature of the superconducting transition of thin films with a layer thickness of 100 nm was measured to be 14.1 K in zero magnetic field.

For the shielded samples S1 and S2, quasiparticle traps were fabricated by first cleaning the Al surface by means of argon plasma milling at  $p = 0.2$  mtorr and *in situ* evaporation of 25 nm Ti and 100 nm Au films at a base pressure of  $\sim 10^{-7}$  torr.

Care was taken to remove resist mask residues after each electron beam writing step using a remote oxygen plasma etch at a pressure of 1 mbar.

We show the scanning electron microscope images of the devices investigated in Supplementary Fig. 1 and define the fabrication parameters in Supplementary Table 1.

**Measurement set-up.** The measurements were performed in a Leiden Cryogenics CF-1200 dry dilution refrigerator with a base temperature of 12 mK equipped with Cu/Ni shielded twisted pair cables thermally anchored at all stages of the refrigerator.

The current bias and gate voltage were applied through battery operated and optically isolated sources to reduce line interference. Similarly, the first stage of the  $V_{\text{sd}}$  amplifier was isolated from the commercial readout electronics. Filtering of the measurement lines was achieved by room temperature LC  $\pi$  filters with a cutoff frequency of  $\sim 100$  MHz followed by a sequence of a high-frequency copper powder filter<sup>31</sup> and a two-pole RC filter with a nominal  $f_{-3\text{dB}} = 50$  kHz, both thermally anchored to the 12 mK stage.

Special care was taken to avoid stray microwave radiation by using outer and inner copper shields enclosing the device. The inner surface of both shields was treated with commercially available Aeroglaze Z306 paint to absorb far-infrared stray radiation<sup>32</sup>. We note that the inner shield was not present for device N.

The switching current histograms were acquired using a Rigol DG4062 arbitrary waveform generator controlling the isolated current bias source with a triangular wave signal, resulting in a  $dI/dt$  current ramp. A finite voltage response

above the preset  $V_{\text{ref}} \sim 10 \mu\text{V}$  triggers the recording of  $I_{\text{sw}}$  (Supplementary Fig. 2c). We note that the delay of the low-pass filters was accounted for on the basis of circuit simulations. Subsequent  $I_{\text{sw}}$  measurements were taken by setting zero  $I_{\text{bias}}$  for approximately 100 ms in between to avoid overheating effects. We did not observe a difference in the switching current histograms taken with waiting times in the range between 20 ms and 10 s.

The schematics of the measurement and typical waveforms are shown in Supplementary Fig. 2.

**Basic characterization of the CPT.** We estimate the charging energy,  $E_c = e^2/2C$ , based on the periodicity of characteristic resonances visible for  $eV_{\text{sd}} = \Delta_{\text{Al}} \dots 2\Delta_{\text{Al}}$ . We attribute these lines to resonant Andreev tunnelling through single levels of the CPT (ref. 33). The resonances occur with a vertical periodicity of  $eV_{\text{sd}} = 2E_c$  and the onset defines  $eV_{\text{sd}} = \Delta_{\text{Al}}$  as well.

The onset of quasiparticle transport is defined by  $eV_{\text{sd}} = 2(\Delta_{\text{NbTiN}} + \Delta_{\text{Al}})$ , which then defines  $\Delta_{\text{NbTiN}}$ . Typical  $I(V)$  and  $dI/dV(V)$  traces are shown in Supplementary Fig. 3 and the recovered parameters are tabulated in Supplementary Table 2.

We evaluate the Josephson coupling for a single tunnel junction<sup>34</sup>:

$$E_j = \frac{\hbar}{2e^2} \frac{\Delta_{\text{Al}}}{R_N/2} K \left( \sqrt{1 - \left( \frac{\Delta_{\text{Al}}}{\Delta_{\text{NbTiN}}} \right)^2} \right)$$

with  $K(x)$  being the complete elliptic integral of the first kind. This expression is valid in the zero-temperature limit, assuming symmetric tunnel junctions with a resistance of  $R_N/2$ .

Alternatively, we can estimate the  $E_j/E_c$  ratio based on the modulation of  $I_{\text{sw}}$  as a function of the gate charge,  $n_g$  (last column of Supplementary Table 2)<sup>35</sup>. We find a good agreement between the  $E_j/E_c$  values acquired by the two independent methods. Finally, we provide  $\delta E(E_c, E_j)$  in the main text based on ref. 36.

## References

- Mueller, F. *et al.* Printed circuit board metal powder filters for low electron temperatures. *Rev. Sci. Instrum.* **84**, 044706 (2013).
- Persky, M. J. Review of black surfaces for space-borne infrared systems. *Rev. Sci. Instrum.* **70**, 2193–2217 (1999).
- Toppari, J. J. *et al.* Cooper-pair resonances and subgap Coulomb blockade in a superconducting single-electron transistor. *Phys. Rev. B* **76**, 172505 (2007).
- Ambegaokar, V. & Baratoff, A. Tunneling between superconductors. *Phys. Rev. Lett.* **10**, 486–489 (1963).
- Matveev, K. A., Gisselält, M., Glazman, L. I., Jonson, M. & Shekhter, R. I. Parity-induced suppression of the Coulomb blockade of Josephson tunneling. *Phys. Rev. Lett.* **70**, 2940–2943 (1993).
- Lutchyn, R. M. Effect of quantum fluctuations on even–odd energy difference in a Cooper-pair box. *Phys. Rev. B* **75**, 212501 (2007).